Ligand-induced chirality in asymmetric CdSe/CdS nanostructures: a close look at chiral tadpoles

Junjie Hao, Yiwen Li, Jun Miao, Rulin Liu, Jiagen Li, Haochen Liu, Qiushi Wang, Huan Liu, Marie-Hélène Delville, Tingchao He, et al.

Ligand-Induced Chirality in Asymmetric CdSe/CdS Nanostructures: A Close Look at Chiral Tadpoles

Junjie Hao,[†,§,⊥,#] Yiwen Li,[†,¶,#] Jun Miao,[Σ,#] Rulin Liu,[‡] Jiagen Li,[‡] Haochen Liu,[§] Qiushi Wang,[†] Huan Liu,[∥] Marie-Hélène Delville,[⊥] Tingchao He,[∥,] Kai Wang,[§,*] Xi Zhu,[‡,*] and Jiaji Cheng[†,*]*

[†]School of Materials Science and Engineering, Hubei University, Wuhan, 430062, China

[‡]Shenzhen Institute of Artificial Intelligence and Robotics for Society (AIRS), Shenzhen, Guangdong, 518172, China

[§]Department of Electrical and Electronic Engineering, Southern University of Science and Technology, Shenzhen, 518055, China

[∥]College of Physics and Optoelectronic Engineering, Shenzhen University, Shenzhen, 518060, China

[¶]Department of Chemistry, Purdue University, West Lafayette, IN, 47907, United States

[⊥]CNRS, Univ. Bordeaux, Bordeaux INP, ICMCB, UMR 5026, Pessac, F-33608, France

[Σ]Institute of Energy and Climate Research (IEK) Photovoltaics, Forschungszentrum Jülich, 52425 Jülich, Germany

*Address correspondence to jiajicheng@hubu.edu.cn, zhuxi@cuhk.edu.cn, wangk@sustc.edu.cn, tche@szu.edu.cn

ABSTRACT

Ligand-induced chirality in asymmetric CdSe/CdS core-shell nanocrystals (NCs) has been extensively applied in chiral biosensors, regioselective syntheses and assemblies, circularly polarized luminescence (CPL) and chiroptic-based devices due to their excellent physiochemical properties, such as the tunable quantum confinement effects, surface functionality and chemical stability. Herein, we present CdSe/CdS NCs with various morphologies such as nanoflowers, tadpoles and dot/rods (DRs) with chirality induced by surface chiral ligands. The observed circular dichroism (CD) and CPL activities are closely associated with the geometrical characteristics of the nanostructures, such as the shell thickness and the aspect ratio of the CdSe/CdS NCs. Furthermore, *in situ* observations of the growth of tadpoles with a single tail indicate that the CD response is mainly attributed to the CdS shell, which has a maximum tail length of ~45 nm (approximately λ/10 of the incident light wavelength). On the other hand, the CPL activity is only related to the CdSe core, and the activity benefits from a thin CdS shell with a relatively high photoluminescence quantum yield (QY). Further theoretical models demonstrated the aspect-ratio-dependent *g*-factor and QY variation in these asymmetric nanostructures. These findings provide insights into not only the asymmetric synthesis of CdSe/CdS NCs, but also the rational design of CdSe/CdS nanostructures with tunable CD and CPL activities.

KEYWORDS: ligand-induced chirality, CdSe/CdS core-shell nanocrystals, circularly polarized luminescence, circular dichroism, nanoflowers, tadpoles

Since the first synthesis of core-shell CdSe/CdS quantum dots (QDs) with featured photoluminescence (PL) properties, many efforts have been made to explore the diversity of shape-controlled CdSe/CdS QDs using different synthetic approaches, cadmium sources, capping ligands, solvents *etc.* Indeed, a variety of morphologies such as spheres,[1] rods,[2] plates,[3] and tetrapods,[4] have been fabricated so far with fine systematic control over the synthesis process. However, the demand from scientists to fundamentally extend the range of shape-controlled synthesis methods and to develop unique physicochemical properties for material designs has had considerable growth concerning to the great potential of these quantum materials in the areas of nanoscience, bionanotechnology and optoelectronics.[5-14] On the other hand, ligand-induced chirality in nanostructures such as metal nanocrystals (NCs) and clusters,[15-19] QDs,[20-23] carbon-based materials[24-26] and semiconductors[27-33] has revolutionized the concept of basic light-matter interactions into a chiroptics realm where more sophisticated phenomena such as circular dichroism (CD) and circularly polarized luminescence (CPL) are dominant.[34-36] With postsynthetic ligand exchanges, the optical chirality can be transferred to the NCs *via* ligand-metal interactions. This chirality is highly sensitive to the size, morphology and surface chemistry of the NCs,[37-43] indicating that ligand-induced chiroptical responses of the NCs can be involved from the bench-top synthesis stage, providing critical information about the shape evolution as well as the ligand-particle interactions during NC formation.[44, 45]

Herein, we present a facile method for the synthesis of CdSe/CdS NCs with various anisotropic shapes including nanoflowers, tadpoles with one to three tails, and dot/rods (DRs) that exhibit tunable absorption and luminescence properties, as illustrated in **Figure 1**. The induced chiroptical properties of these nanostructures are investigated through CD and CPL spectrometers to elucidate the geometric effects (such as the shell thickness and length-to-diameter ratio) on the ligand-

induced chirality of CdSe/CdS-based NCs. Furthermore, *in situ* CD/CPL observations during the formation of chiral tadpoles are applied to reveal the growth mechanism as well as the tail length effect on the chiroptical responses of CdSe/CdS tadpoles. With these investigations, we hope to broaden the scope of CdSe/CdS-based synthesis methods to furnish products with various asymmetric morphologies and to gain new insights into the relationship between ligand-induced chirality at the molecular level and geometrical effects of QDs at the nanoscale.

RESULTS AND DISCUSSION

Synthesis of CdSe/CdS NCs with various anisotropic shapes

To obtain chiroptical properties, anisotropic CdSe/CdS NCs are first synthesized in the organic phase with different morphologies and then postsynthetically ligand-exchanged with L/D-cysteine to obtain L- or D-Cys-CdSe/CdS NCs in the aqueous phase, as indicated in the experimental section. Typically, the morphology of the CdSe/CdS NCs is finely tuned by shape-directing agents, as observed by transmission electron microscopy (TEM) in **Figure 2 (a-f)**, in which the geometrical parameters for each nanostructure are measured for more than 100 NCs and summarized in **Table S1**. As a result, a variety of nanoshapes, including nanoflowers, tadpoles with one to three tails, named Tadpole-I, Tadpole-II and Tadpole-III hereafter, and DRs can be obtained at the nanometric scale by adjusting the amount and chemical nature of the ligands. Note that we use wurtzite CdSe (w-CdSe) as the core material, as shown in **Figure 2 (a-2, d-2 and e-2)**, and wurtzite CdS shells (~0.36 nm corresponding to the d-spacing of [100] planes) preferentially formed in all of the core-shell NCs, which is in agreement with the reference, which states that CdS prefers to grow in the wurtzite phase from w-CdSe seeds.[4] Alivisatos[46] and Cheon[5] also showed that the surface energy of the NCs can be modulated by introducing surfactants that

adsorb onto the different surfaces of the growing crystallites. As surfactants stabilize a given surface by "selective adhesion", the growth rate difference between the different crystallographic directions can be accentuated.

At low concentrations or in the absence of additional alkylphosphonic acid ligands (n-octadecylphosphonic acid (ODPA) or n-hexylphosphonic acid (HPA)) (**Figure 2 (a-c)**), spherical NCs are more likely to form, which results in nanoflowers, Tadpole-III, and Tadpole-II shapes in our system. The formation of petals in CdSe/CdS nanoflowers (**Figure 2a**) may be due to the presence of ligands such as ODPA and HPA on the surface of the w-CdSe core, which played a certain anisotropic role, making it different from uniform spherical CdSe/CdS NCs, as reported in a previous study.[47] Some similar work also showed that nanoflowers can be formed by assembling small building blocks such as ZnO monodispersed nanoflowers.[48] In addition, the ratio of ODPA and OA is also an important factor[49] for the formation of different shapes because of the different growth kinetics[50] of cadmium phosphate and cadmium carboxylate. Due to the relatively low proportion of ODPA in Tadpole-III and Tadpole-II, the role of highly reactive OA is still dominant, meaning that a large amount of CdS nuclei may quickly form and grow on the spherical CdSe core, and then ODPA plays a role in anisotropic tail growth. In contrary, with increasing the "selective adhesion" ligands (ODPA or HPA), Tadpole-I and DR shapes can be formed because the [100] and [110] surfaces are more favorable than the other surfaces for adhesion, leading to the growth of shells along the [001] direction to form long tail or rod-like shapes.

The corresponding UV-vis absorption and PL spectra of CdSe/CdS nanostructures and their PL emission peak positions together with their full-width at half-maximum (FWHMs) values are shown in **Figure S1** and **Table S1** before ligand exchange and in **Figure 2 (g)** and **Table 1** after this same ligand exchange. Apparently, after the CdS shell growth, the absorption peak of the CdSe

cores redshifted from 539 nm to 605, 606, 605, 606, 568 and 572 nm for the different morphologies (**Table S1**), along with an increase in the PL quantum yield (QY) from 1.5% to 49% simply because the CdS shell repairs the defects on the surface of CdSe cores (**Table S1**). To avoid redundancy, the shell thickness was selected as a variable in this study. As shown in **Tables 1** and **S1**, the shell thickness of DR-1 is only 0.2 nm, which produces a small redshift (25 nm). In contrast, the shell thickness of Tadpole-I is 4.3 nm, which produces a large redshift (77 nm). The DR-2, Tadpole-II, and Tadpole-III shapes are all in agreement with the change rule of the PL redshift caused by the increase in shell thickness, but the case of nanoflowers is not completely consistent, which may be caused by the gaps between petals. The QY of different NCs gradually decreases as the shell layers increase (**Figure S2 (a)**) due to the defects and lattice mismatch of the shell, which is consistent with the literature as well.[47, 51] Moreover, as shown in **Figure S2 (b)** and **Table S2**, the FWHM value increases with increases in the standard deviation (SD) ratio, which indicates that a uniform size distribution is more likely to achieve a narrower FWHM. Additionally, after ligand exchange, the PL and UV spectra of the NCs have only a slight blueshift of 1-3 nm, as shown in **Figure 2 (g)** and **Table 1**, which indicates that the process of ligand exchange did not cause the aggregation or destruction of NCs. The crystalline structure of the synthesized CdSe/CdS core/shell Tadpole-I was then characterized by X-ray diffraction (XRD) measurements. As shown in **Figure 2 (h)**, the XRD spectra and corresponding diffraction peaks of cores and tadpoles match well with w-CdSe (JCPDF No. 02-0330) and w-CdS (JCPDF No. 41-1049), respectively. The results demonstrate that as the shells grow thicker, the crystalline structures were changed from pure w-CdSe crystals to pure w-CdS, and the diffraction peaks, such as (100), (101) and (110), show a slight shift towards larger 2θ directions due to the smaller lattice plane spacing of CdS shells.

Table 1. CD and CPL Anisotropy Factors of D-Cys-CdSe/CdS NCs in Water

Name	Shell-thickness (nm)[a]	Ratio[c]	PL (nm)[d]	$\lvert g_{CD+} - g_{CD-}\rvert/2$[e]	QY(%)[f]	g_{lum}/λ_{CPL} (nm)[g]
Nanoflower	**8.7**	**1.2**	**624**	$\mathbf{0.68\times10^{-5}}$	**2**	/
Tadpole-III	**8.1**[b]	**1.8**	**632**	$\mathbf{1.79\times10^{-5}}$	**8**	/
Tadpole-II	**7.1**[b]	**1.9**	**633**	$\mathbf{4.41\times10^{-5}}$	**12**	$\mathbf{1.71\times10^{-4}/636.9}$
Tadpole-I-1	**4.3**[b]	**3.8**	**629**	$\mathbf{9.79\times10^{-5}}$	**37**	$\mathbf{5.12\times10^{-4}/632.9}$
DR-1	**0.2**	**2.7**	**577**	$\mathbf{9.36\times10^{-5}}$	**44**	$\mathbf{8.46\times10^{-4}/584.9}$
DR-2	**1.0**	**12.4**	**583**	$\mathbf{39.18\times10^{-5}}$	**39**	$\mathbf{7.45\times10^{-4}/585.8}$

[a]The CdS shell thickness around the CdSe core. [b]The shell thickness of the head of the tadpoles. [c]Ratio of the total length to the largest diameter of the nanostructures. [d]PL emission peak position of Cys-CdSe/CdS NCs in the water phase. [e]Magnitude of the g_{CD} factor, defined as $|g_{CD+} - g_{CD-}|/2$. [f]PL QY of the NCs after ligand exchange. [g]CPL of anisotropic g_{lum} at the most intense CPL wavelength (nm).

Study of the ligand-induced chirality of CdSe/CdS NCs

Since the first observation of CD responses in CdS QDs capped with chiral molecules,[52] studies of chiral CdSe/CdS NCs with ligand-induced chirality have rapidly increased in the past decade, with a focus on the origin of chirogenesis, CPL and biological applications. However, as shown in **Table S3** (details are shown in Supplementary Information), the current CD and CPL studies for chiral cadmium-based NCs induced by small chiral ligands are still incomplete, with accessibility issues with CPL instruments and insufficient theoretical/experimental support for understanding the chirality induction mechanism. Therefore, although the underlying mechanism is still unclear, in this work, we focus on the study of CdSe/CdS NCs with different morphologies to tentatively reveal the change trends in the CD and CPL, as shown below.

After proper ligand exchange, electronic CD measurements were then employed to study the chiroptical properties of the cysteine-functionalized CdSe/CdS NCs. In the vicinity of the exciton absorption of each nanostructure, mirrored CD line shapes are presented when L- and D-cysteine are separately used as surface ligands (**Figures 3 (a-f)** and **S3**). To quantitatively compare the CD responses in these nanostructures, their anisotropic *g*-factors[53] are calculated and exhibited in **Figure S3,** where the highest value of the *g*-factor, defined as $|g_{CD}^{-} - g_{CD}^{+}|/2$,[22] is used as an indicator for the magnitude of the induced chirality (**Tables 1** and **S4**). Note that all the nanostructures share the same batch of CdSe cores with the same ligand exchange treatment. We then assume that the differences in the CD spectra were mainly related to the geometry-induced variations in the nanostructures. For a more in-depth analysis, the CD and UV spectra were divided basically into two regions: the 400-500 nm region where the CdS absorption dominates and the 500-700 nm region where CdSe core absorption dominates. With this consideration, nanoflower- (**Figure 3 (a)**), tadpole- (**Figure 3 (b-d)**) and long DR- (**Figure 3 (f)**) shaped samples show only CdS CD activity because they have relatively thick shells (> 1 nm) with a large volume of CdS, while short DRs (**Figure 3 (e)**) with thin shells still show a CD response corresponding to the CdSe core, which agrees with our previous work on chiral CdSe/CdS DRs.[22] It is particularly worth mentioning that Tadpole-I is able to maintain a high CD activity, as shown in **Figure 3d**, which may be due to its special anisotropic morphology, even if the shell thickness is large (>10 monolayers). Moreover, considering the CD responses of the CdS shell, the anisotropic g_{abs}-factor maximum (~ 470 nm, **Figure S3, Table 1**) basically increases as the morphology evolves from nanoflower to tadpole and then DRs, indicating asymmetric morphologies. This means that a large aspect ratio (AR) provides an induced CD response, as chirality is strongly related to the degree of symmetry breaking (σ, i, C_n or S_n). Similar to Tang[20] and Kuang's[54] work on chiral quantum

rods, the induced chirality can be recognized as the array of Cd-S bonds in the direction of the long axis of the asymmetric NCs. The total effective number of cysteine molecules increases to some extent as the AR (or the NC length) increases, resulting in enhanced chiral coupling, which gives rise to stronger CD intensity. Nonetheless, this tendency is not applicable for the band-edge absorption in DRs (**Figure S4**). At the band edge, this CD activity is mainly due to the CdSe core, and increasing the length of the chiral NCs (**Figure S4**) results in a decrease in the CD intensity because of the thick CdS shell, which blocks the chiral interactions between the CdSe core and the chiral ligands. Note that Purcell-Milton *et al.*[55] claimed that two competing effects may occur when increasing the shell thickness: first, increasing the distance between ligands and holes localized in the CdSe core would decrease their coupling effects, and accordingly, the CdS shell would act as an energy barrier for the holes; second, the subsequent addition of the CdS layers reduces the hole energy and the hole level closer to the energetic resonance of the HOMO of the ligand which increases the CD response. Our observations are in good agreement with the first effect, even though the mechanism is still unclear.

Furthermore, the corresponding CPL activities of these samples are shown in **Figures 4** and **S5** with the g_{lum}-factor,[56] defined as $g_{lum} = 2(I_L - I_R)/(I_L + I_R)$, where I_L and I_R are the emission intensities of left- and right- handed polarized light, respectively, increases in the order of nanoflowers (**Figure 4 (a)**), tadpoles (**Figure 4 (b-d)**) and DRs (**Figure 4 (e and f)**). The CPL behavior of these samples also exhibits an inverse dependency on the CdS shell thickness, but is proportional to the photoluminescence QY, as summarized in **Table 1 and Figure 5**. The same trend can be observed in the L-Cys-CdSe/CdS NCs (**Table S5**). As stated before, we assert that the number of chiral interactions between the CdSe cores and the chiral surface ligands would

determine the intensity of CPL that can be achieved, indicating that a thin CdS shell is favorable for obtaining strong CPL signals.

***In-situ* observations of the formation of chiral Tadpole-I**

To further investigate the induced chiral responses of these asymmetric nanostructures, chiral Tadpole-I is chosen as a typical sample for *in-situ* observations during the formation of its tail. As illustrated by the TEM images in **Figure 6**, chiral Tadpole-I is formed step-by-step *via* site-selective growth of the CdS tail from a spherical CdSe/CdS QDs. This process can be divided into two steps. First, due to the high reaction temperature (320 °C), a wurtzite-phase spherical CdS shell (< 2 min) is formed[4, 5] due to the high reactivity of cadmium carboxylates.[57] As a result, the CD measurements exhibit relatively weak activities just after ligand exchange. Afterwards, with further tail growth, the CD intensity changes from almost inactive to active as confirmed by the corresponding CD and UV spectra (**Figure 6**) and anisotropic *g*-factors (**Figure S6**), which is attributed to CdS tail formation. Indeed, since the shell becomes thicker by a factor of 4 (from 1.0 nm to 4.3 nm), it exhibits a decreasing possibility for ligand and core interactions and, therefore, any chirality transfer between the two (**Tables 2 and S6**).[55] The absorption of CdSe (500-700 nm) becomes weaker to nearly null, while the absorption for CdS becomes stronger with a shoulder appearing at approximately 470 nm along with PL peaks redshifted from 554 to 631 nm (**Figure S7, Table S7**).[47, 58] Due to the strong complexing ability of the phosphonate group, which coordinates to three or more cation centers, instead of one (or two) for the carboxylate group,[57, 59] the alkylphosphonic acid ligands (ODPA) selectively bind to the [100] and [110] surfaces, facilitating growth along the [001] direction to gradually favor long tail formation. This anisotropic shape explains the variation in the chiroptical signals in tadpoles during growth, which is in

agreement with previous statements that thin shells facilitate core-ligand interactions and that asymmetric morphologies benefit the induced CD responses in the CdS shell absorption region.

Table 2. CD Anisotropy Factors of D-Cys-CdSe/CdS Tadpole-I at Different Reaction Times

Name	Shell thickness (nm)[a]	Ratio[b]	PL (nm)[c]	$\lvert g_{CD+} - g_{CD-} \rvert / 2$[d]	QY(%)[e]
Tadpole-I-2	**0.9**	**1.0**	**572**	$\mathbf{0.75\times10^{-5}}$	**2**
Tadpole-I-3	**1.0**	**1.0**	**581**	$\mathbf{0.59\times10^{-5}}$	**6**
Tadpole-I-4	**1.3**	**1.5**	**596**	$\mathbf{0.98\times10^{-5}}$	**8**
Tadpole-I-5	**3.6**	**2.4**	**614**	$\mathbf{5.57\times10^{-5}}$	**17**
Tadpole-I-1	**4.3**	**3.8**	**629**	$\mathbf{9.79\times10^{-5}}$	**37**

[a]The shell thickness of the tadpole heads. [b]Ratio of the total length to the largest diameter of the nanostructures. [c]PL emission peak position of Cys-CdSe/CdS NCs in the water phase. [d]Magnitude of the g_{CD} factor, defined as $|g_{CD+} - g_{CD-}|/2$. [e]PL QY of the NCs after the ligand exchange.

However, further growth of the tail does not necessarily result in enhanced CD activity. **Figures 7** and **S8** demonstrate that when the length of the tail grows even longer (from 22.5 to 180.8 nm), the recorded CD responses become weaker with a gradual redshift in the PL and UV spectra (**Figure S9, Table S8**).[47, 58] Considering that only when nanostructures are much smaller than the incident light wavelength (typically $\lambda/10$), the weak spatial dispersion theory can be applied. Under these circumstances, local effects dominate, and nonlocal effects can introduce chirality coefficients, which can be recognized as a manifestation of first-order spatial dispersion, and the homogenization of the microscopic Maxwell equations can be applied.[60] When the length of the chiral Tadpole-I reaches a value that is one tenth of the incident wavelength (for example, approximately 40-50 nm), a further increase in the length would not necessarily further enhance

the chirality, indicating that interparticle interactions would account for the overall chirality at this point. This phenomenon is effectively what we observe, wherein the *g*-factor of the system increases as the tail length increases and reaches a maximum at a tail length of ~45 nm (Tadpole-I-1) and then decreases with an even longer tail length (**Tables 3, S8 and S9**). It is, however, worth noting that a related article reported that for rod-like QDs, a proper length with twice the exciton Bohr radius would achieve the strongest CD signals, although this tendency is not obviously observed in this work.[20]

We also investigated the CPL behavior of the corresponding NCs **(Figures 8**, **S10 and Table 3)**, and observed that the overall g_{lum} decreased straightforwardly as the tail length increased, with the highest g_{lum} of 5.71×10^{-4} for Tadpole-I-6 (22.5 nm). Tadpole-I-2 to Tadpole-I-4 showed a nearly inactive CPL response due to a quenching effect (a low PL QY) during ligand exchange even though they have a thinner CdS shell than the other structures. Because CPL measures the emission property of the CdSe/CdS nanostructures, the greater the increase in the tail length is, the more difficult it is for ligand chirality induction, even though a longer tail may introduce some degree of geometrical anisotropy for CD increments, as previously stated. Interestingly, although the geometrical relationships are still complex, the best way to obtain multiple CPL and CD line shapes with high intensity is to achieve chiral tadpoles such as Tadpole-I with a thin shell with a reasonable QY for the photoluminescent core (Tadpole-I-6, $g_{lum} = 5.71\times10^{-4}$) and a moderate tail length/AR for the CdS tail (Tadpole-I-1, $g_{CD} = 9.79\times10^{-5}$), as indicated by **Table 3**. The best parameters to obtain CD and CPL activities are in fact not necessarily the same, and the same trend can be observed in L-Cys-CdSe/CdS Tadpole-I (**Table S10**). These observations could provide critical information for the rational design of CdSe/CdS Tadpole-I structures with tunable chiroptical activities, which should also be applicable for other related asymmetric

multidimensional morphologies, such as DRs and tetrapods, since hole level-chiral ligand interactions are always the key issue in chiral quantum semiconductor heterostructures.[61]

Table 3. CD and CPL Anisotropy Factors of D-Cys-CdSe/CdS Tadpole-I with Different Lengths.

Name	Shell-thickness (nm)[a]	Ratio[b]	PL (nm)[c]	$\lvert g_{CD+} - g_{CD-} \rvert/2$[d]	QY(%)[e]	g_{lum}/λ_{CPL} (nm)[f]
Tadpole-I-6	**3.3**	**2.4**	**613**	$\mathbf{5.60\times10^{-5}}$	**20**	$\mathbf{5.71\times10^{-4}/613.7}$
Tadpole-I-7	**4.2**	**2.6**	**624**	$\mathbf{7.71\times10^{-5}}$	**28**	$\mathbf{5.32\times10^{-4}/625.4}$
Tadpole-I-1	**4.3**	**3.8**	**629**	$\mathbf{9.79\times10^{-5}}$	**37**	$\mathbf{5.12\times10^{-4}/632.9}$
Tadpole-I-8	**6.1**	**7.3**	**639**	$\mathbf{5.41\times10^{-5}}$	**13**	$\mathbf{2.38\times10^{-4}/638.7}$
Tadpole-I-9	**9.2**	**8.6**	**640**	$\mathbf{4.03\times10^{-5}}$	**11**	$\mathbf{1.02\times10^{-4}/647.2}$

[a]The shell thickness of the tadpole heads. [b]Ratio of the total length to the largest diameter of the nanostructures. [c]PL emission peak position of Cys-CdSe/CdS NCs in the water phase. [d]Magnitude of the g_{CD} factor, defined as $|g_{CD+} - g_{CD-}|/2$. [e]PL QY of the NCs after ligand exchange. [f]CPL anisotropic g_{lum} at the most intense CPL wavelength (nm).

Simulation of the AR-dependent g-factor and the QY variation

The g-factor. To better understand the chiral origin and simulate the chiroptical behavior of our tadpole system, a brief theoretical modeling strategy is presented as follows (Detailed deductions and calculations about the *g*-factor and the QY can be found in the Supplementary Information): Since the chirality is induced *via* the attachment of the organic chiral ligands on the outer surface, it is calculated using the London equation for the penetration of the ligand field. The magnetic field is believed to come from the directed movement of electrons in the ligand when excited. The field then couples with the excited moving electrons in the QDs, and therefore affects their

excitations since the excitations of the ligands are chiral. Thus, the penetration of the magnetic field into the QD surface can describe the injection of chirality into the QDs. For the semiconductor case, the term $i\omega\tau$ in the conductivity σ is much smaller than 1, *i.e.,* $i\omega\tau \ll 1$, and can be ignored. Thus,

$$\nabla \times \frac{\partial j}{\partial t} = \frac{ne^2}{m}\left(-\frac{\partial B}{\partial t}\right) \Rightarrow \nabla^2 B = \frac{\mu n e^2}{m} B = \lambda_s^{-2} B,$$

$$B(r) = B_0 exp\left(-\frac{R-r}{\lambda_s}\right),$$

where $\lambda_s = \sqrt{\frac{m}{\mu n e^2}}$ is the penetration depth, r is the distance from the center of the QD, R is the radius, μ is the permeability, n is the density of the electrons, and m is the effective mass of electrons. Since this magnetic field penetration decays exponentially, CD injection must also be performed. Given the speed of light c, the intensity of this injected electromagnetic wave injected by the chiral ligand is calculated as:

$$I = \frac{B^2 c}{2\mu} = \frac{B_0^2 c}{2\mu} exp\left(-2\frac{R-r}{\lambda_s}\right).$$

The calculation of the chiral dichroism of the spherical structure considers both the decay of the light intensity along the incident direction and its interaction with the electron flux above. Thus,

$$CD_{sphere}(\omega, R) \propto \int_0^R \int_0^{2\sqrt{R^2-r^2}} 2\pi r e^{-\frac{x}{\lambda}} e^{-2\frac{R-r}{\lambda_s}} dx dr,$$

where λ is the wavelength of the incident light. In this way, the calculated results of cysteine-capped CdSe/CdS nanostructures with different shell thicknesses are illustrated in **Figure 9 (a)**, in which both the *g*-factor and the QY show a good correlation with our experimental results and

match with previously published data reported by Purcell-Milton *et al*.[55] For the tadpole, similarly, since there is no difference in n along the z direction, it is simpler than the spherical case:

$$CD_{tadpole}(\omega, l) \propto \int_0^l e^{-\frac{z}{\lambda}} dz,$$

where $\lambda \approx \frac{c_{light}}{2\kappa\omega}$, κ is the imaginary part of the complex refractive index, R is the radius of the tadpole head, and l is the length of the tadpole tail. A further assumption made is that $\kappa \approx \sqrt{\epsilon_2}$ and that ϵ_2 increases first with the length of the tadpole tail and then converges to the bulk value of the material.

The quantum yield. According to the work of Singh,[62] both the QYs of singlet and triplet ϕ_D are proportional to the exciton diffusion length L_D, *i.e.* $\phi_D \propto L_D^2$. Since the exciton diffusion length is proportional to the size of the QDs, it can be assumed to be a second-order relationship with both the number of shells and the aspect ratio, given that the core and the head of the tadpole barely change in size. **Figure 9 (b)** shows the corresponding calculated *g*-factor and QY curves fitted with our experimental data on a series of Tadpole-I structures with different AR values. As expected, the calculation demonstrates the AR effect on the *g*-factor and QY, however, it should be noted that when Tadpole-I grows even longer, the interparticle interactions should be taken into account as well.

CONCLUSION

In conclusion, cysteine-capped chiral asymmetric CdSe/CdS nanostructures with tunable morphologies were synthesized using the shape-directing ligands. The measurements of induced chiroptical activities of these nanostructures showed that: 1) the induced CD intensity of the CdSe

core existed only in the short DR sample, which is due to the barrier effect of the CdS shell (>1.0 nm); 2) the symmetry breaking effect also accounted for the CD responses, and asymmetric samples with larger ARs or longer lengths would be beneficial for the CD activities; 3) the step-by-step growth mechanism of Tadpole-I was investigated, confirming that increasing the tail length enhanced the CD intensity; however, further growth of the tail length (> λ/10) attenuated the chiroptical responses because interparticle interactions affected the overall chirality; and 4) CPL measurements were applied in parallel, showing that the chiral-ligand-photoluminescent-core interactions were the key indicator for CPL performance. In general, asymmetric samples with thin CdS shells and a high PL QY were the most efficient in terms of CPL activities. However, a sample with the highest CD performance does not necessarily also exhibit an efficient CPL response.

These findings prove that induced CD and CPL can serve as indicators of the extent to which a chiral ligand can affect the hole wave function through an energy barrier such as a CdS shell with different morphologies,[61] and we expect these observations to provide experimental support for the manipulating the chirality of CdSe/CdS-based nanostructures with potential uses in stereoselective catalysis, chiroptical sensing and chirality-based devices for both optics and biological applications.[13, 14, 33, 63-69]

METHODS

Chemicals

Tri-n-octylphosphine oxide (TOPO, 99%), tri-n-octylphosphine (TOP, 97%), tributylphosphine (TBP, 99%), n-octadecylphosphonic acid (ODPA, 97%) and n-hexylphosphonic acid (HPA, 97%) were purchased from Strem Chemicals. Cadmium oxide (CdO, 99.99%), sulfur (S, 99.98%) and selenium (Se, 99.99%) were purchased from Sigma-Aldrich. Oleic acid (OA, AR), L-cysteine

hydrochloride monohydrate (L-Cys, 99%), D-cysteine hydrochloride monohydrate (D-Cys, 98%) and tetramethylammonium hydroxide solution (TMAH, AR, 25 wt. % in H_2O) were purchased from Aladdin Industrial Co., Ltd. (Shanghai, China). Deionized (DI) water was purchased from Hangzhou Wahaha Group Co., Ltd, China. All chemicals were used as received without further purification.

Synthesis of the CdSe core

The synthesis procedure was based on the procedure reported in the literature.[2, 70] Typically, TOPO (1.5 g), ODPA (0.140 g) and CdO (0.030 g) were mixed in a 50 mL flask, heated to 150 °C and alternately exposed to vacuum conditions and an argon atmosphere at least 5 times until CdO was a brown solid and the remaining reagents were a colorless liquid. Then, to dissolve the CdO, the solution was heated to above 320 °C under argon until it became optically clear and colorless, which indicated that the reaction between CdO and ODPA was complete. Then, the temperature was increased to 350 °C, and 1.5 mL of TOP was injected into the flask, which caused the temperature to naturally decrease to 300 °C. Then, a Se:TOP solution (0.4 mL, 1 mol/L) was injected into the flask at 380 °C and was allowed to react for several seconds. The size of the CdSe core could be adjusted by altering the temperature and reaction time.

Purification and acidification of the CdSe-TOP core

The reaction mixture was cooled to 70~80 °C, and a certain amount of TBP and 4 mL of ethanol were added into the above solution for the purification process; the mixture was centrifuged at 10000 rpm for 3 min. Then, the precipitate was dissolved in a small amount of toluene, and the supernatant was discarded. After centrifugation was performed again, the precipitate was redispersed in TOP (CdSe-TOP).

Synthesis of CdSe/CdS tadpole NCs

In a typical synthesis of CdSe/CdS tadpole NCs *via* seeded growth, CdO (115.8 mg) was mixed in a 50 mL flask together with TOPO (3 g), ODPA (285 mg) and OA (1.02 ml). After alternately exposing the flask to vacuum conditions and an argon atmosphere at least 5 times at 150 °C, the resulting solution was heated to 320 °C to cause the solution to become a completely transparent liquid without any solids. Then, 1.5 mL of TOP was added; the temperature recovered to 320 °C and 50 nmol of CdSe was added. The sulfur-tri-n-octylphosphine (S-TOP, 0.5 M, 3 mL) was divided into four injections at 2-min intervals (0 min, 2 min, 4 min, and 6 min). The CdSe/CdS NCs were allowed to grow for approximately 8 min after the injection. Finally, the reaction mixture was cooled to room temperature, and an extraction procedure was performed to separate the NCs from the side products and unreacted precursors. Tadpoles NCs with different tail lengths were used by adding different amounts of CdSe core, ranging from 5 nmol to 200 nmol.

Synthesis of CdSe/CdS NCs with different shapes

Different shapes of NCs can be synthesized just by changing the ligands. By changing the ratio of ODPA and OA, different shapes can be obtained, such as nanoflower, Tadpole-III, Tadpole-II, Tadpole-I, and DRs. For different lengths of DRs, different ratios of HPA were added instead of OA.

Ligand exchange of the CdSe/CdS NCs with chiral cysteine molecules

The cysteine ligand exchange reaction was carried out using a previously reported method[21] with some modifications. Cysteine hydrochloride monohydrate (702.52 mg) was dissolved in DI water (40 mL, [Cys] = 0.1 M). The pH of the resulting solution was adjusted to 12.0 with TMAH solution (AR, 25 wt. % in H_2O). A solution of CdSe/CdS NCs in n-hexane (5 mL, 1×10^{-6} M) was added to

the cysteine solution (5 mL), and the reaction mixture was deoxygenated and stirred at room temperature under argon in the absence of light for 72 h. The reaction mixture was left to stand for 1 h to allow the phases to separate. The bottom aqueous layer was taken with a syringe, and the Cys-CdSe/CdS NCs were purified 5 times with DI H_2O by using ultra centrifugal filter units (Millipore, 10,000 d, 15 mL). The purified Cys-NCs were diluted and dispersed in DI water and stored at room temperature in the dark.

Structural and optical characterization

The UV/vis absorption spectrum of each sample was measured using a TU-1901 double-beam UV/vis spectrophotometer (Beijing Purkine General Instrument Co. Ltd., China), and the PL spectra were recorded on a fluoroSENS spectrophotometer (Gilden Photonics). The absolute PL QYs of the NC solutions were measured using an Ocean Optics FOIS-1 integrating sphere coupled with a QE65 Pro spectrometer. CD measurements were conducted on a JASCO J-1500 CD spectrometer. The scan rate was 20 nm/min. All CD experiments were carried out in Milli-Q water with a quartz cuvette (0.1 cm path length, Hellma). CPL measurements were performed on a JASCO CPL-300 spectrometer in Milli-Q water with a quartz cuvette (0.1 cm path length, Hellma) with an excitation wavelength of 400 nm. All optical measurements were performed at room temperature under ambient conditions. TEM images were collected using a FEI Tecnai G2 F30 microscope, and X-ray diffraction was measured by a Bruker Advance D8 Ew (Germany).

ASSOCIATED CONTENT

Supporting Information

Additional data and figures are included in the Supplementary Information. These data describe the UV-vis absorptions and PL spectra of the different morphologies (Figures S1, S7, and S9), the

relationship between PL spectra and shapes of different NCs (Figure S2), CD spectra and the corresponding anisotropic g_{CD} factor variation with wavelength (Figures S3, S4, S6, and S8), and the g_{lum} value variation with the wavelength of the morphologies exhibiting CPL activity (Figures S5, and S10). Theoretical calculations and modeling of the *g*-factor and QY (Figures S11 and S12). Table S1. Physical properties of NCs with different shapes in the organic phase. Table S2. Diameter standard deviation ratio study of NCs with different shapes. Table S3. CD anisotropy *g*-factors and CPL g_{lum} for chiral cadmium-based NCs induced by small-molecule chiral ligands. Table S4. CD anisotropy factors of D-Cys-CdSe/CdS NCs. Table S5. CPL anisotropy factors of L-Cys-CdSe/CdS NCs in water. Table S6. CD anisotropy factors of D-Cys-CdSe/CdS Tadpole-I for different reaction times. Table S7. Physical properties of tadpoles at different reaction times in the organic phase. Table S8. Physical properties of tadpoles with different lengths in organic phase. Table S9. CD anisotropy factors of D-Cys-CdSe/CdS Tadpole-I with different lengths. Table S10. CPL anisotropy factors of L-Cys-CdSe/CdS Tadpole-I with different lengths. This material is available free of charge *via* the Internet at http://pubs.acs.org.

AUTHOR INFORMATION

Corresponding Author:

Tingchao He: tche@szu.edu.cn

Kai Wang: wangk@sustc.edu.cn

Xi Zhu: zhuxi@cuhk.edu.cn

Jiaji Cheng: jiajicheng@hubu.edu.cn

Author Contributions

[#]J. Hao, Y. Li and J. Miao contributed equally to this work. All authors contributed to the writing of this manuscript and have approved the final version of the manuscript.

Notes

The authors declare no competing financial interest.

ACKNOWLEDGMENT

The work was supported by National Natural Science Foundation of China (No. 61875082), National Key Research and Development Program (Nos. 2017YFE0120400 and 2016YFB0401702), Natural Science Foundation of Guangdong Province (2019A1515012094), Shenzhen Basic Research Project of Science and Technology (JCYJ20190808121211510). Funding from Shenzhen Institute of Artificial Intelligence and Robotics for Society (AIRS) is appreciated. TEM data were obtained using equipment maintained by Southern University of Science and Technology Core Research Facilities, and the authors would like to acknowledge the technical support from Dongsheng He and Yang Qiu in SUSTech CRF.

REFERENCES

(1) Chen, O.; Zhao, J.; Chauhan, V. P.; Cui, J.; Wong, C.; Harris, D. K.; Wei, H.; Han, H.-S.; Fukumura, D.; Jain, R. K.; Bawendi, M. G. Compact High-Quality CdSe–CdS Core–Shell Sanocrystals with Narrow Emission Linewidths and suppressed Blinking. *Nature Materials* **2013,** *12* (5), 445-451.

(2) Carbone, L.; Nobile, C.; De Giorgi, M.; Sala, F. D.; Morello, G.; Pompa, P.; Hytch, M.; Snoeck, E.; Fiore, A.; Franchini, I. R.; Nadasan, M.; Silvestre, A. F.; Chiodo, L.; Kudera, S.; Cingolani, R.; Krahne, R.; Manna, L. Synthesis and Micrometer-Scale Assembly of Colloidal CdSe/CdS Nanorods Prepared by a Seeded Growth Approach. *Nano Lett.* **2007,** *7* (10), 2942-2950.

(3) Gao, X.; Zhang, X.; Zhao, L.; Huang, P.; Han, B.; Lv, J.; Qiu, X.; Wei, S.-H.; Tang, Z. Distinct Excitonic Circular Dichroism between Wurtzite and Zincblende CdSe Nanoplatelets. *Nano Lett.* **2018,** *18* (11), 6665-6671.

(4) Talapin, D. V.; Nelson, J. H.; Shevchenko, E. V.; Aloni, S.; Sadtler, B.; Alivisatos, A. P. Seeded Growth of Highly Luminescent CdSe/CdS Nanoheterostructures with Rod and Tetrapod Morphologies. *Nano Lett.* **2007,** *7* (10), 2951-2959.

(5) Jun, Y.-w.; Choi, J.-s.; Cheon, J. Shape Control of Semiconductor and Metal Oxide Nanocrystals through Nonhydrolytic Colloidal Routes. *Angew. Chem. Int. Ed.* **2006,** *45* (21), 3414-3439.

(6) Algar, W. R.; Susumu, K.; Delehanty, J. B.; Medintz, I. L. Semiconductor Quantum Dots in Bioanalysis: Crossing the Valley of Death. *Anal. Chem.* **2011,** *83* (23), 8826-8837.

(7) Waiskopf, N.; Ben-Shahar, Y.; Galchenko, M.; Carmel, I.; Moshitzky, G.; Soreq, H.; Banin, U. Photocatalytic Reactive Oxygen Species Formation by Semiconductor–Metal Hybrid Nanoparticles. Toward Light-Induced Modulation of Biological Processes. *Nano Lett.* **2016,** *16* (7), 4266-4273.

(8) Dai, X.; Zhang, Z.; Jin, Y.; Niu, Y.; Cao, H.; Liang, X.; Chen, L.; Wang, J.; Peng, X. Solution-Processed, High-Performance Light-Emitting Diodes Based on Quantum Dots. *Nature* **2014,** *515* (7525), 96-99.

(9) Meinardi, F.; Colombo, A.; Velizhanin, K. A.; Simonutti, R.; Lorenzon, M.; Beverina, L.; Viswanatha, R.; Klimov, V. I.; Brovelli, S. Large-Area Luminescent Solar Concentrators Based on 'Stokes-Shift-Engineered' Nanocrystals in a Mass-Polymerized PMMA Matrix. *Nat. Photonics* **2014,** *8* (5), 392-399.

(10) Panfil, Y. E.; Oded, M.; Banin, U. Colloidal Quantum Nanostructures: Emerging Materials for Display Applications. *Angew. Chem. Int. Ed.* **2018,** *57* (16), 4274-4295.

(11) Pavlopoulos, N. G.; Dubose, J. T.; Liu, Y.; Huang, X.; Pinna, N.; Willinger, M.-G.; Lian, T.; Char, K.; Pyun, J. Type I *vs.* Quasi-Type II Modulation in CdSe@CdS Tetrapods: Ramifications for Noble Metal Tipping. *CrystEngComm* **2017,** *19* (43), 6443-6453.

(12) Mishra, N.; Lian, J.; Chakrabortty, S.; Lin, M.; Chan, Y. Unusual Selectivity of Metal Deposition on Tapered Semiconductor Nanostructures. *Chem. Mater.* **2012,** *24* (11), 2040-2046.

(13) Sun, M.; Xu, L.; Qu, A.; Zhao, P.; Hao, T.; Ma, W.; Hao, C.; Wen, X.; Colombari, F. M.; de Moura, A. F.; Kotov, N. A.; Xu, C.; Kuang, H. Site-Selective Photoinduced Cleavage and Profiling of DNA by Chiral Semiconductor Nanoparticles. *Nat. Chem.* **2018,** *10* (8), 821-830.

(14) Li, S.; Liu, J.; Ramesar, N. S.; Heinz, H.; Xu, L.; Xu, C.; Kotov, N. A. Single- and Multi-Component Chiral Supraparticles as Modular Enantioselective Catalysts. *Nat. Commun.* **2019,** *10* (1), 4826.

(15) Cheng, J.; Hill, E. H.; Zheng, Y.; He, T.; Liu, Y. Optically Active Plasmonic Resonance in Self-Assembled Nanostructures. *Mater. Chem. Front.* **2018,** *2*, 662-678.
(16) Ben-Moshe, A.; Maoz, B.; Govorov, A. O.; Markovich, G. Chirality and Chiroptical Effects in Inorganic Nanocrystal Systems with Plasmon and Exciton Resonances. *Chem. Soc. Rev.* **2013,** *42* (16), 7028-7041.
(17) Wang, X.; Tang, Z. Circular Dichroism Studies on Plasmonic Nanostructures. *Small* **2017,** *13* (1), 1601115.
(18) Noguez, C.; Garzon, I. L. Optically Active Metal Nanoparticles. *Chem. Soc. Rev.* **2009,** *38* (3), 757-771.
(19) Guerrero-Martínez, A.; Alonso-Gómez, J. L.; Auguié, B.; Cid, M. M.; Liz-Marzán, L. M. From Individual to Collective Chirality in Metal Nanoparticles. *Nano Today* **2011,** *6* (4), 381-400.
(20) Gao, X.; Zhang, X.; Deng, K.; Han, B.; Zhao, L.; Wu, M.; Shi, L.; Lv, J.; Tang, Z. Excitonic Circular Dichroism of Chiral Quantum Rods. *J. Am. Chem. Soc.* **2017,** *139* (25), 8734-8739.
(21) Tohgha, U.; Deol, K. K.; Porter, A. G.; Bartko, S. G.; Choi, J. K.; Leonard, B. M.; Varga, K.; Kubelka, J.; Muller, G.; Balaz, M. Ligand Induced Circular Dichroism and Circularly Polarized Luminescence in CdSe Quantum Dots. *ACS Nano* **2013,** *7* (12), 11094-11102.
(22) Cheng, J.; Hao, J.; Liu, H.; Li, J.; Li, J.; Zhu, X.; Lin, X.; Wang, K.; He, T. Optically Active CdSe-Dot/CdS-Rod Nanocrystals with Induced Chirality and Circularly Polarized Luminescence. *ACS Nano* **2018,** *12* (6), 5341-5350.
(23) Elliott, S. D.; Moloney, M. P.; Gun'ko, Y. K. Chiral Shells and Achiral Cores in CdS Quantum Dots. *Nano Lett.* **2008,** *8* (8), 2452-2457.
(24) Li, F.; Li, Y.; Yang, X.; Han, X.; Jiao, Y.; Wei, T.; Yang, D.; Xu, H.; Nie, G. Highly Fluorescent Chiral N-S-Doped Carbon Dots from Cysteine: Affecting Cellular Energy Metabolism. *Angew. Chem. Int. Ed.* **2018,** *57* (9), 2377-2382.
(25) Nakakuki, Y.; Hirose, T.; Sotome, H.; Miyasaka, H.; Matsuda, K. Hexa-Peri-Hexabenzo[7]Helicene: Homogeneously Π-Extended Helicene as a Primary Substructure of Helically Twisted Chiral Graphenes. *J. Am. Chem. Soc.* **2018,** *140* (12), 4317-4326.
(26) Đorđević, L.; Arcudi, F.; D'Urso, A.; Cacioppo, M.; Micali, N.; Bürgi, T.; Purrello, R.; Prato, M. Design Principles of Chiral Carbon Nanodots Help Convey Chirality from Molecular to Nanoscale Level. *Nat. Commun.* **2018,** *9* (1), 3442.
(27) Cleary, O.; Purcell-Milton, F.; Vandekerckhove, A.; Gun'ko, Y. K. Chiral and Luminescent TiO_2 Nanoparticles. *Adv. Opt. Mater.* **2017,** *5* (16), 1601000.
(28) Jiang, S.; Chekini, M.; Qu, Z. B.; Wang, Y. C.; Yeltik, A.; Liu, Y. G.; Kotlyar, A.; Zhang, T. Y.; Li, B.; Demir, H. V.; Kotov, N. A. Chiral Ceramic Nanoparticles and Peptide Catalysis. *J. Am. Chem. Soc.* **2017,** *139* (39), 13701-13712.
(29) Dong, Y.; Zhang, Y.; Li, X.; Feng, Y.; Zhang, H.; Xu, J. Chiral Perovskites: Promising Materials toward Next-Generation Optoelectronics. *Small* **2019,** *15* (39), 1902237.
(30) Long, G.; Sabatini, R.; Saidaminov, M. I.; Lakhwani, G.; Rasmita, A.; Liu, X.; Sargent, E. H.; Gao, W. Chiral-Perovskite Optoelectronics. *Nature Reviews Materials* **2020,** *5*, 423–439.
(31) Yeom, J.; Santos, U. S.; Chekini, M.; Cha, M.; de Moura, A. F.; Kotov, N. A. Chiromagnetic Nanoparticles and Gels. *Science* **2018,** *359* (6373), 309-314.
(32) Li, Y.; Cheng, J.; Li, J.; Zhu, X.; He, T.; Chen, R.; Tang, Z. Tunable Chiroptical Properties from the Plasmonic Band to Metal-Ligand Charge Transfer Band of Cysteine-Capped Molybdenum Oxide Nanoparticles. *Angew. Chem. Int. Ed.* **2018,** *57* (32), 10236-10240.

(33) Hao, C.; Gao, R.; Li, Y.; Xu, L.; Sun, M.; Xu, C.; Kuang, H. Chiral Semiconductor Nanoparticles for Protein Catalysis and Profiling. *Angew. Chem. Int. Ed.* **2019,** *58* (22), 7371-7374.
(34) Zhao, X.; Zang, S.-Q.; Chen, X. Stereospecific Interactions between Chiral Inorganic Nanomaterials and Biological Systems. *Chem. Soc. Rev.* **2020,** *49*, 2481-2503.
(35) Ma, W.; Xu, L.; de Moura, A. F.; Wu, X.; Kuang, H.; Xu, C.; Kotov, N. A. Chiral Inorganic Nanostructures. *Chem. Rev.* **2017,** *117* (12), 8041-8093.
(36) Naito, M.; Iwahori, K.; Miura, A.; Yamane, M.; Yamashita, I. Circularly Polarized Luminescent CdS Quantum Dots Prepared in a Protein Nanocage. *Angew. Chem. Int. Ed.* **2010,** *49* (39), 7006-7009.
(37) Yan, J.; Feng, W.; Kim, J.-Y.; Lu, J.; Kumar, P.; Mu, Z.; Wu, X.; Mao, X.; Kotov, N. A. Self-Assembly of Chiral Nanoparticles into Semiconductor Helices with Tunable near-Infrared Optical Activity. *Chem. Mater.* **2020,** *32* (1), 476-488.
(38) Ji, B.; Panfil, Y. E.; Waiskopf, N.; Remennik, S.; Popov, I.; Banin, U. Strain-Controlled Shell Morphology on Quantum Rods. *Nat. Commun.* **2019,** *10* (1), 2.
(39) Gallagher, S. A.; Moloney, M. P.; Wojdyla, M.; Quinn, S. J.; Kelly, J. M.; Gun'ko, Y. K. Synthesis and Spectroscopic Studies of Chiral CdSe Quantum Dots. *J. Mater. Chem.* **2010,** *20* (38), 8350-8355.
(40) Varga, K.; Tannir, S.; Haynie, B. E.; Leonard, B. M.; Dzyuba, S. V.; Kubelka, J.; Balaz, M. CdSe Quantum Dots Functionalized with Chiral, Thiol-Free Carboxylic Acids: Unraveling Structural Requirements for Ligand-Induced Chirality. *ACS Nano* **2017,** *11* (10), 9846-9853.
(41) Huo, S.; Duan, P.; Jiao, T.; Peng, Q.; Liu, M. Self-Assembled Luminescent Quantum Dots to Generate Full-Color and White Circularly Polarized Light. *Angew. Chem.* **2017,** *129* (40), 12342-12346.
(42) Martynenko, I. V.; Baimuratov, A. S.; Osipova, V. A.; Kuznetsova, V. A.; Purcell-Milton, F.; Rukhlenko, I. D.; Fedorov, A. V.; Gun'ko, Y. K.; Resch-Genger, U.; Baranov, A. V. Excitation Energy Dependence of the Photoluminescence Quantum Yield of Core/Shell CdSe/CdS Quantum Dots and Correlation with Circular Dichroism. *Chem. Mater.* **2018,** *30* (2), 465-471.
(43) Choi, J. K.; Haynie, B. E.; Tohgha, U.; Pap, L.; Elliott, K. W.; Leonard, B. M.; Dzyuba, S. V.; Varga, K.; Kubelka, J.; Balaz, M. Chirality Inversion of CdSe and CdS Quantum Dots without Changing the Stereochemistry of the Capping Ligand. *ACS Nano* **2016,** *10* (3), 3809-3815.
(44) Jiang, W.; Qu, Z.-b.; Kumar, P.; Vecchio, D.; Wang, Y.; Ma, Y.; Bahng, J. H.; Bernardino, K.; Gomes, W. R.; Colombari, F. M.; Lozada-Blanco, A.; Veksler, M.; Marino, E.; Simon, A.; Murray, C.; Muniz, S. R.; de Moura, A. F.; Kotov, N. A. Emergence of Complexity in Hierarchically Organized Chiral Particles. *Science* **2020,** *368* (6491), 642-648.
(45) Govorov, A. O.; Fan, Z.; Hernandez, P.; Slocik, J. M.; Naik, R. R. Theory of Circular Dichroism of Nanomaterials Comprising Chiral Molecules and Nanocrystals: Plasmon Enhancement, Dipole Interactions, and Dielectric Effects. *Nano Lett.* **2010,** *10* (4), 1374-1382.
(46) Manna, L.; Scher, E. C.; Alivisatos, A. P. Synthesis of Soluble and Processable Rod-, Arrow-, Teardrop-, and Tetrapod-Shaped CdSe Nanocrystals. *J. Am. Chem. Soc.* **2000,** *122* (51), 12700-12706.
(47) Nan, W.; Niu, Y.; Qin, H.; Cui, F.; Yang, Y.; Lai, R.; Lin, W.; Peng, X. Crystal Structure Control of Zinc-Blende CdSe/CdS Core/Shell Nanocrystals: Synthesis and Structure-Dependent Optical Properties. *J. Am. Chem. Soc.* **2012,** *134* (48), 19685-19693.

(48) Zhang, S.; Chen, H.-S.; Matras-Postolek, K.; Yang, P. ZnO Nanoflowers with Single Crystal Structure Towards Enhanced Gas Sensing and Photocatalysis. *Phys. Chem. Chem. Phys.* **2015,** *17* (45), 30300-30306.
(49) Balan, A. D.; Olshansky, J. H.; Horowitz, Y.; Han, H.-L.; O'Brien, E. A.; Tang, L.; Somorjai, G. A.; Alivisatos, A. P. Unsaturated Ligands Seed an Order to Disorder Transition in Mixed Ligand Shells of CdSe/CdS Quantum Dots. *ACS Nano* **2019,** *13* (12), 13784-13796.
(50) Yang, P.; Ando, M.; Taguchi, T.; Murase, N. Highly Luminescent CdSe/$Cd_xZn_{1-x}S$ Quantum Dots with Narrow Spectrum and Widely Tunable Wavelength. *J. Phys. Chem. C* **2011,** *115* (30), 14455-14460.
(51) Coropceanu, I.; Rossinelli, A.; Caram, J. R.; Freyria, F. S.; Bawendi, M. G. Slow-Injection Growth of Seeded CdSe/CdS Nanorods with Unity Fluorescence Quantum Yield and Complete Shell to Core Energy Transfer. *ACS Nano* **2016,** *10* (3), 3295-3301.
(52) Moloney, M. P.; Gun'ko, Y. K.; Kelly, J. M. Chiral Highly Luminescent CdS Quantum Dots. *Chem. Commun.* **2007,** *38*, 3900-3902.
(53) Pescitelli, G.; Di Bari, L.; Berova, N. Conformational Aspects in the Studies of Organic Compounds by Electronic Circular Dichroism. *Chem. Soc. Rev.* **2011,** *40* (9), 4603-4625.
(54) Ma, W.; Mao, J.; Hao, C.; Xu, L.; Xu, C.; Kuang, H. Chiral Semiconductor Nanorod Heterostructures with High Photocatalysis Activity. *Appl. Catal., B* **2019,** *245*, 691-697.
(55) Purcell-Milton, F.; Visheratina, A. K.; Kuznetsova, V. A.; Ryan, A.; Orlova, A. O.; Gun'ko, Y. K. Impact of Shell Thickness on Photoluminescence and Optical Activity in Chiral CdSe/CdS Core/Shell Quantum Dots. *ACS Nano* **2017,** *11* (9), 9207-9214.
(56) Riehl, J. P.; Muller, G., Circularly Polarized Luminescence Spectroscopy and Emission-Detected Circular Dichroism. Berova, N.; Polavarapu, P. L.; Nakanishi, K.; Woody, R. W., Eds. John Wiley & Sons, Inc.: **2012**; Vol. 1, pp 65-90.
(57) Gao, Y.; Peng, X. Crystal Structure Control of CdSe Nanocrystals in Growth and Nucleation: Dominating Effects of Surface *versus* Interior Structure. *J. Am. Chem. Soc.* **2014,** *136* (18), 6724-6732.
(58) Li, J. J.; Wang, Y. A.; Guo, W.; Keay, J. C.; Mishima, T. D.; Johnson, M. B.; Peng, X. Large-Scale Synthesis of Nearly Monodisperse CdSe/CdS Core/Shell Nanocrystals Using Air-Stable Reagents *via* Successive Ion Layer Adsorption and Reaction. *J. Am. Chem. Soc.* **2003,** *125* (41), 12567-12575.
(59) Puri, M.; Ferry, V. E. Circular Dichroism of CdSe Nanocrystals Bound by Chiral Carboxylic Acids. *ACS Nano* **2017,** *11* (12), 12240-12246.
(60) Nanostructured Metamaterials – Exchange between Experts in Electromagnetics and Material Science. Kruglyak, V.; Baas, A. F. d.; Bergmair, I.; Scharf, T.; Tretyakov, S.; Barois, P., Eds. Publications Office of the European Union: Luxembourg:, **2010**; p. 139.
(61) Ben-Moshe, A.; Teitelboim, A.; Oron, D.; Markovich, G. Probing the Interaction of Quantum Dots with Chiral Capping Molecules Using Circular Dichroism Spectroscopy. *Nano Lett.* **2016,** *16* (12), 7467-7473.
(62) Yeboah, D.; Singh, J. Dependence of Exciton Diffusion Length and Diffusion Coefficient on Photophysical Parameters in Bulk Heterojunction Organic Solar Cells. *J. Electron. Mater.* **2017,** *46* (11), 6451-6460.
(63) Ma, W.; Xu, L.; Wang, L.; Xu, C.; Kuang, H. Chirality-Based Biosensors. *Adv. Funct. Mater.* **2019,** *29* (1), 1805512.
(64) Sun, Y.; Zhao, C.; Gao, N.; Ren, J.; Qu, X. Stereoselective Nanozyme Based on Ceria Nanoparticles Engineered with Amino Acids. *Chem. Eur. J.* **2017,** *23* (72), 18146-18150.

(65) Zhan, P.; Wang, Z.-G.; Li, N.; Ding, B. Engineering Gold Nanoparticles with DNA Ligands for Selective Catalytic Oxidation of Chiral Substrates. *ACS Catalysis* **2015,** *5* (3), 1489-1498.
(66) de Q. Silveira, G.; Ramesar, N. S.; Nguyen, T. D.; Bahng, J. H.; Glotzer, S. C.; Kotov, N. A. Supraparticle Nanoassemblies with Enzymes. *Chem. Mater.* **2019,** *31* (18), 7493-7500.
(67) Yuan, A.; Hao, C.; Wu, X.; Sun, M.; Qu, A.; Xu, L.; Kuang, H.; Xu, C. Chiral Cu_xOS@ZIF-8 Nanostructures for Ultrasensitive Quantification of Hydrogen Sulfide *in Vivo*. *Adv. Mater.* **2020,** *32* (19), 1906580.
(68) Zhao, B.; Yu, H.; Pan, K.; Tan, Z. a.; Deng, J. Multifarious Chiral Nanoarchitectures Serving as Handed-Selective Fluorescence Filters for Generating Full-Color Circularly Polarized Luminescence. *ACS Nano* **2020,** *14* (3), 3208–3218.
(69) Li, Y.; Miao, Z.; Shang, Z.; Cai, Y.; Cheng, J.; Xu, X. A Visible- and Nir-Light Responsive Photothermal Therapy Agent by Chirality-Dependent MoO_{3-x} Nanoparticles. *Adv. Funct. Mater.* **2019,** *30* (4), 1906311.
(70) Choi, C. L.; Koski, K. J.; Sivasankar, S.; Alivisatos, A. P. Strain-Dependent Photoluminescence Behavior of CdSe/CdS Nanocrystals with Spherical, Linear, and Branched Topologies. *Nano Lett.* **2009,** *9* (10), 3544-3549.

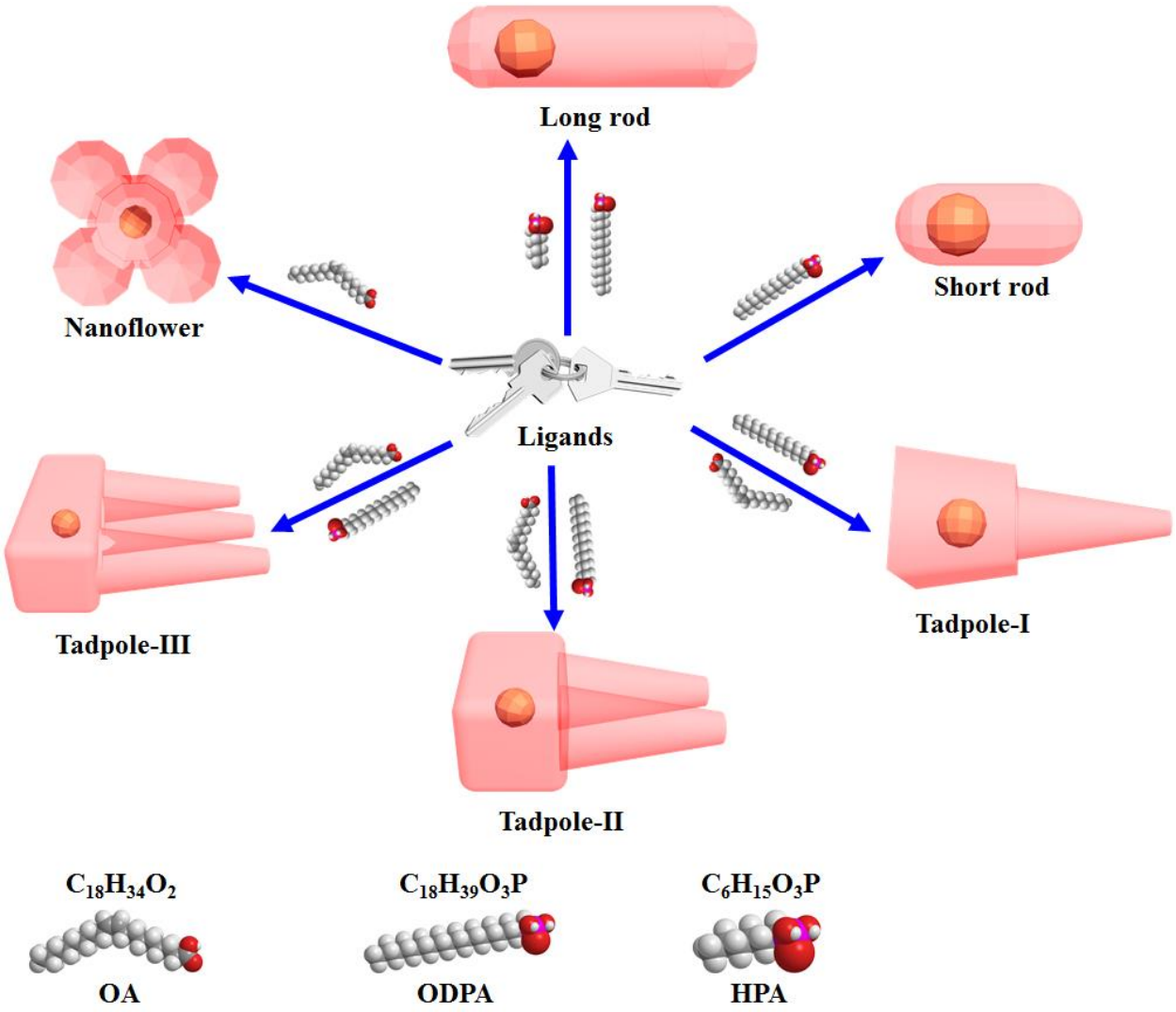

Figure 1. The mechanism of ligand-induced shape variations. By changing the composition of the ligands, various anisotropic shapes such as nanoflowers, tadpoles with one to three tails, and dot/rods can be obtained.

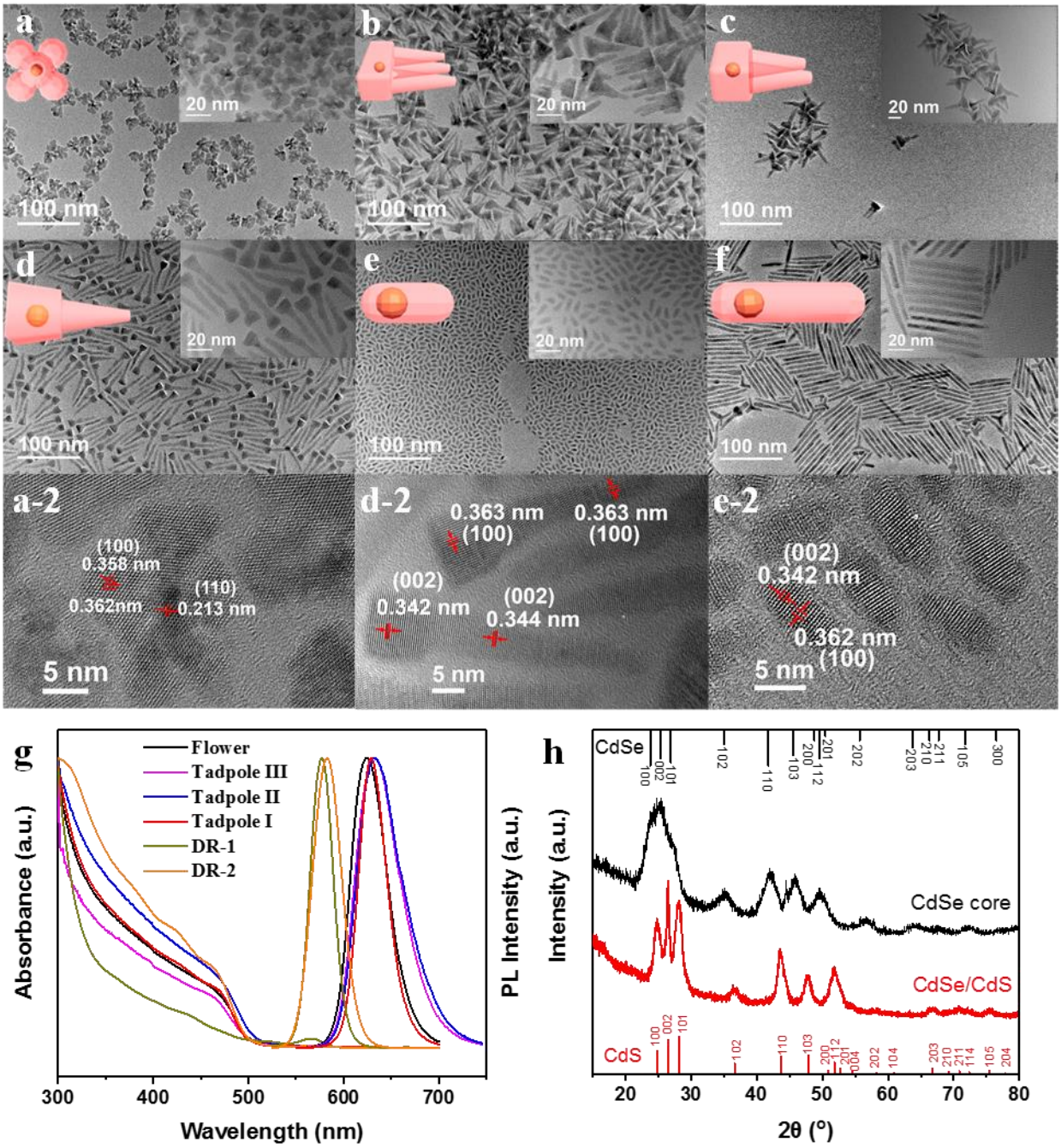

Figure 2. (a-f) TEM and high-resolution TEM (HRTEM) (insert) of CdSe/CdS NCs with different shapes: (a) nanoflowers, (b) Tadpole-III, (c) Tadpole-II, (d) Tadpole-I, (e) short dot/rods, and (f) long dot/rods. (a-2), (d-2) and (e-2) are the corresponding detailed analyses on the lattice fringes. (g) The corresponding UV-vis absorption and PL spectra, under excitation by a 450 nm

monochromatic light, of the different shapes of D-Cys-CdSe/CdS NCs in the water phase. (h) X-ray diffraction (XRD) patterns of powdered samples of CdSe cores (upper line) and CdSe/CdS tadpoles (lower line). The XRD PDF standard cards of CdSe (upper bars, JCPDF of No. 02-0330) and CdS (lower bars, JCPDF of No. 41-1049) are also exhibited with the XRD results, respectively, as references.

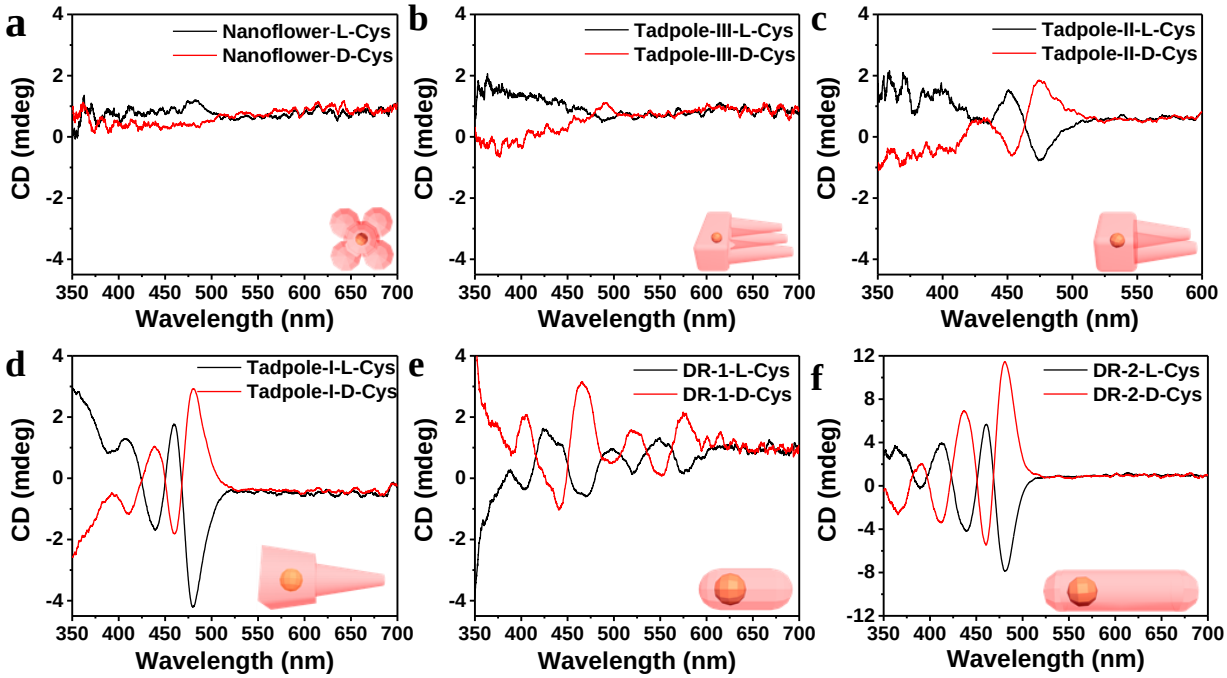

Figure 3. CD spectra of the L-/D- CdSe/CdS NCs with different shapes. (a) Nanoflowers, (b) Tadpole-III, (c) Tadpole-II, (d) Tadpole-I, (e) short dot/rods, and (f) long dot/rods.

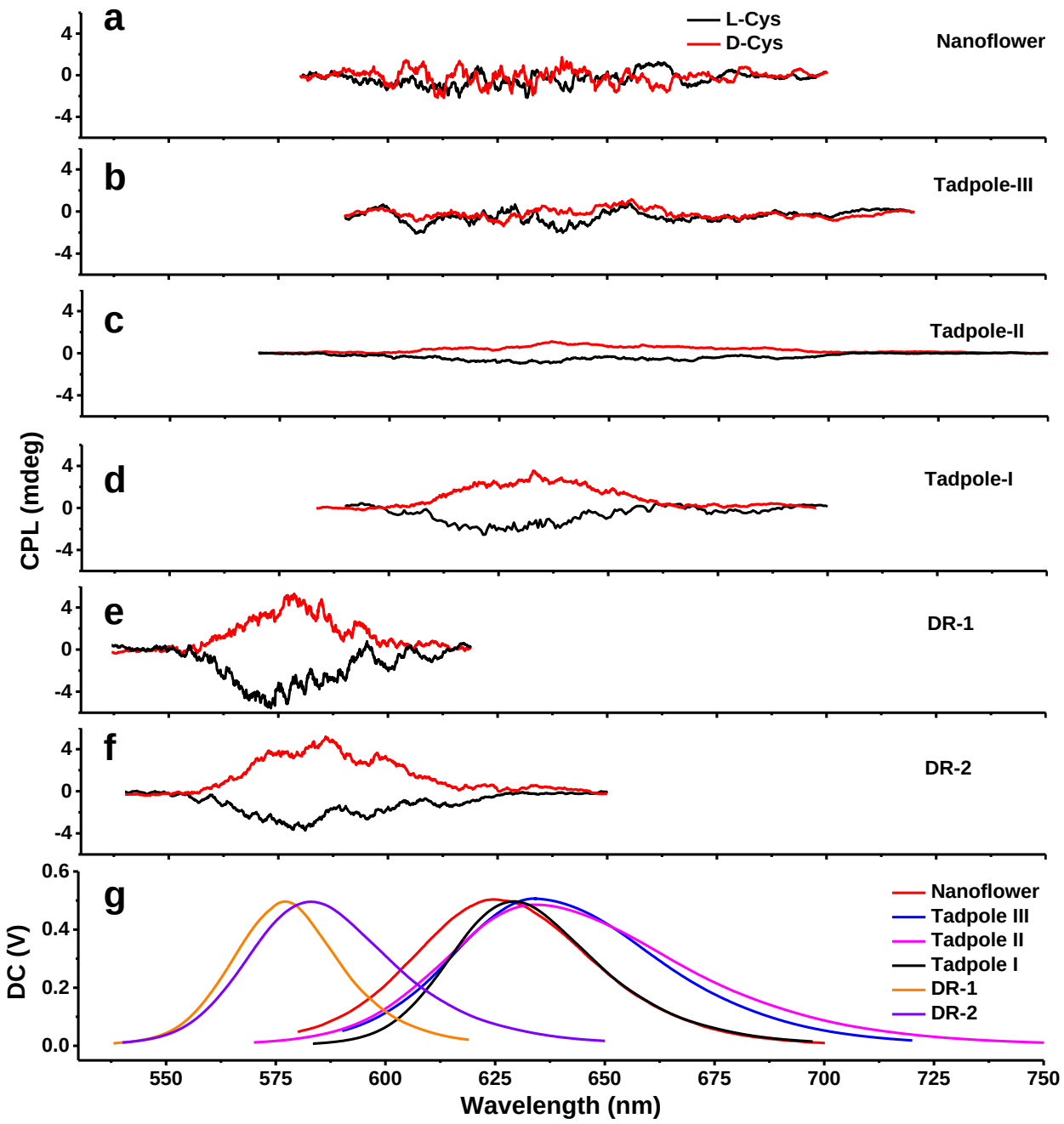

Figure 4. Mirror-image CPL spectra of the CdSe/CdS NCs with different shapes: (a) Nanoflowers, (b) Tadpole-III, (c) Tadpole-II, (d) Tadpole-I, (e) short dot/rods (DR-1), and (f) long dot/rods (DR-2). (g) The corresponding DC spectra of the D-Cys-CdSe/CdS NCs.

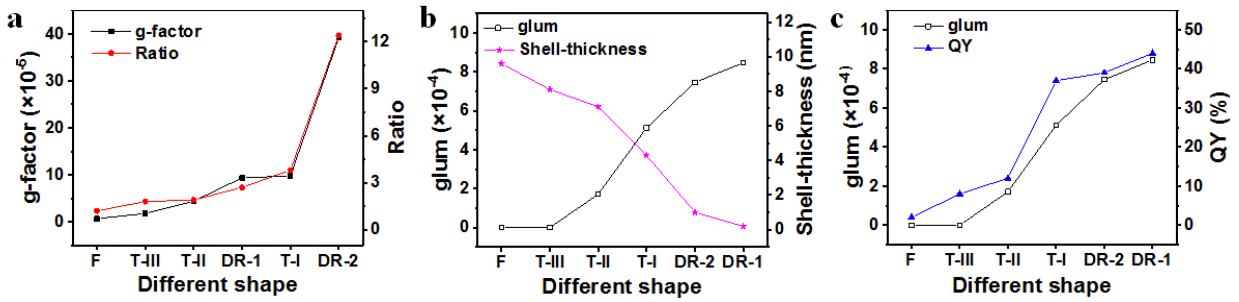

Figure 5. Dependence of CD and CPL anisotropy factors of D-Cys-CdSe/CdS NCs on the different shapes. (a) The dependence of g_{CD} factors of D-Cys-CdSe/CdS NCs on the ratio of the total length to the largest diameter of the nanostructures; (b), (c) the dependence of the g_{lum} factor values of D-Cys-CdSe/CdS NCs on the CdS shell thickness and the photoluminescence QY. (F: Nanoflowers, T-III: Tadpole-III, T-II: Tadpole-II, T-I: Tadpole-I, DR-1: DR-1, DR-2: DR-2)

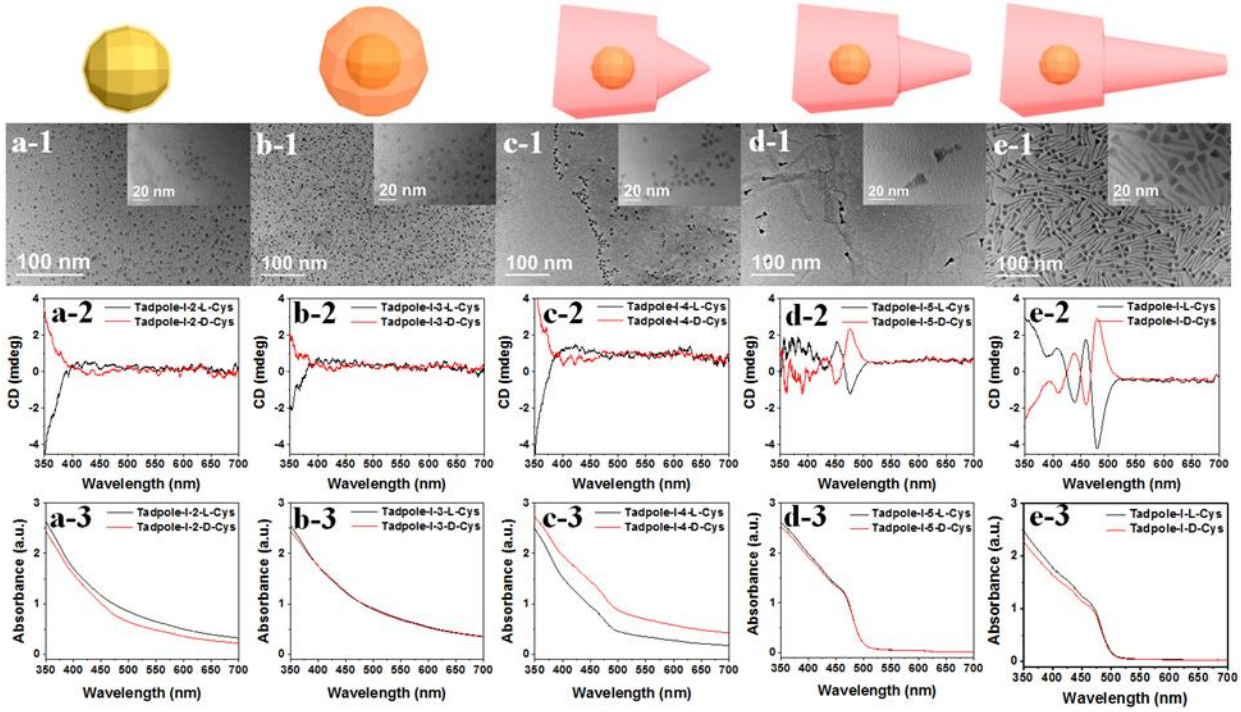

Figure 6. TEM images, CD spectra and UV/vis absorption spectra of the Tadpole-I-shaped CdSe/CdS NC growth evolution process. (a) Tadpole-I-2, 30 s, (b) Tadpole-I-3, 1 min, (c) Tadpole-I-4, 2 min, (d) Tadpole-I-5, 4 min, and (e) Tadpole-I-1, 8 min. (a-1 to e-1) the TEM and

HRTEM images and (a-2 to e-2) CD spectra and (a-3 to e-3) UV/vis absorption spectra of tadpole-shaped NCs at different reaction times.

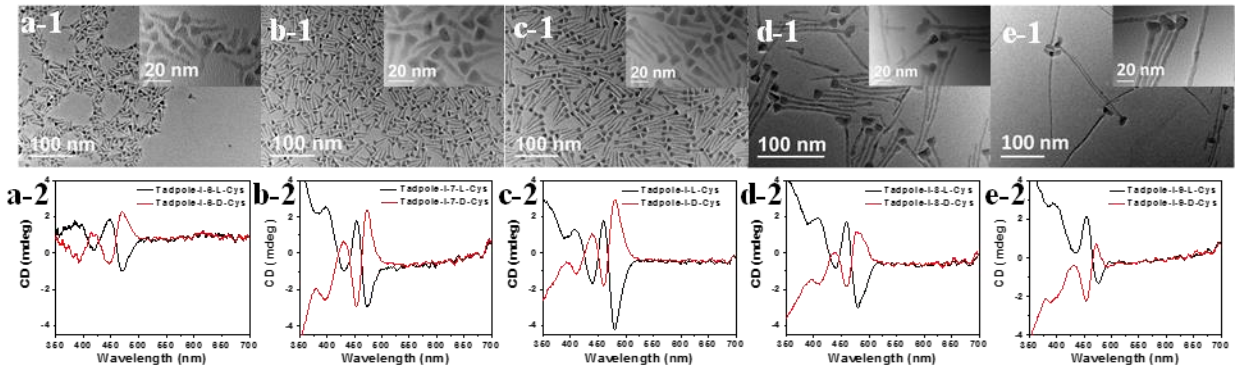

Figure 7. TEM images and CD spectra of Tadpole-I-shaped CdSe/CdS NCs with different lengths. (a) Tadpole-I-6, 22.5 nm, (b) Tadpole-I-7, 30.9 nm, (c) Tadpole-I-1, 43 nm, (d) Tadpole-I-8, 109.5 nm and (e) Tadpole-I-9, 180.8 nm. TEM and HRTEM images (a-1 to e-1) and CD spectra (a-2 to e-2).

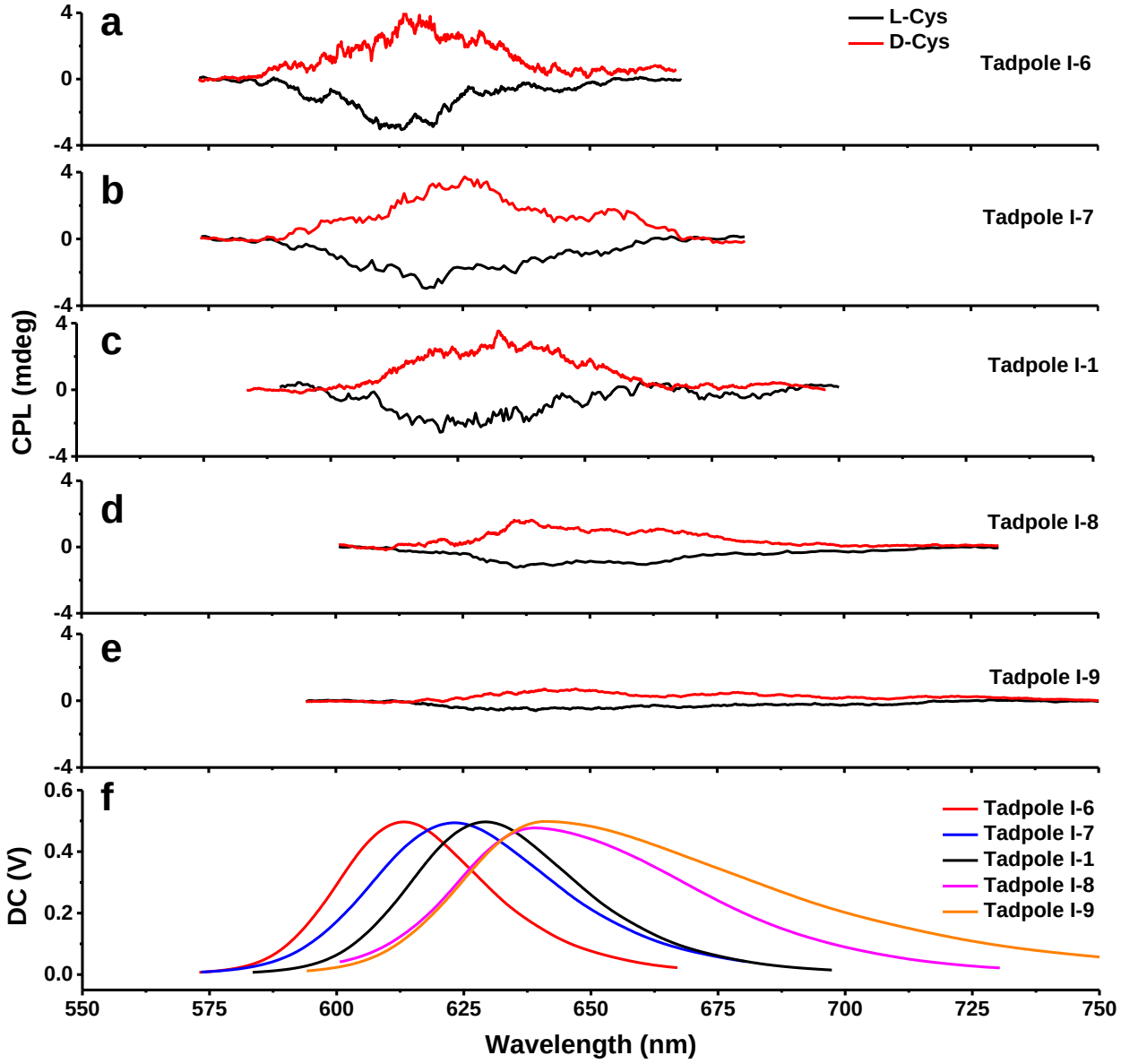

Figure 8. Mirror-image CPL spectra of tadpole-shaped CdSe/CdS NCs with different lengths. (a) Tadpole-I-6, 22.5 nm, (b) Tadpole-I-7, 30.9 nm, (c) Tadpole-I-1, 43 nm, (d) Tadpole-I-8, 109.5 nm and (e) Tadpole-I-9, 180.8 nm. (f) The corresponding DC spectra of D-Cys-CdSe/CdS Tadpole-I NCs.

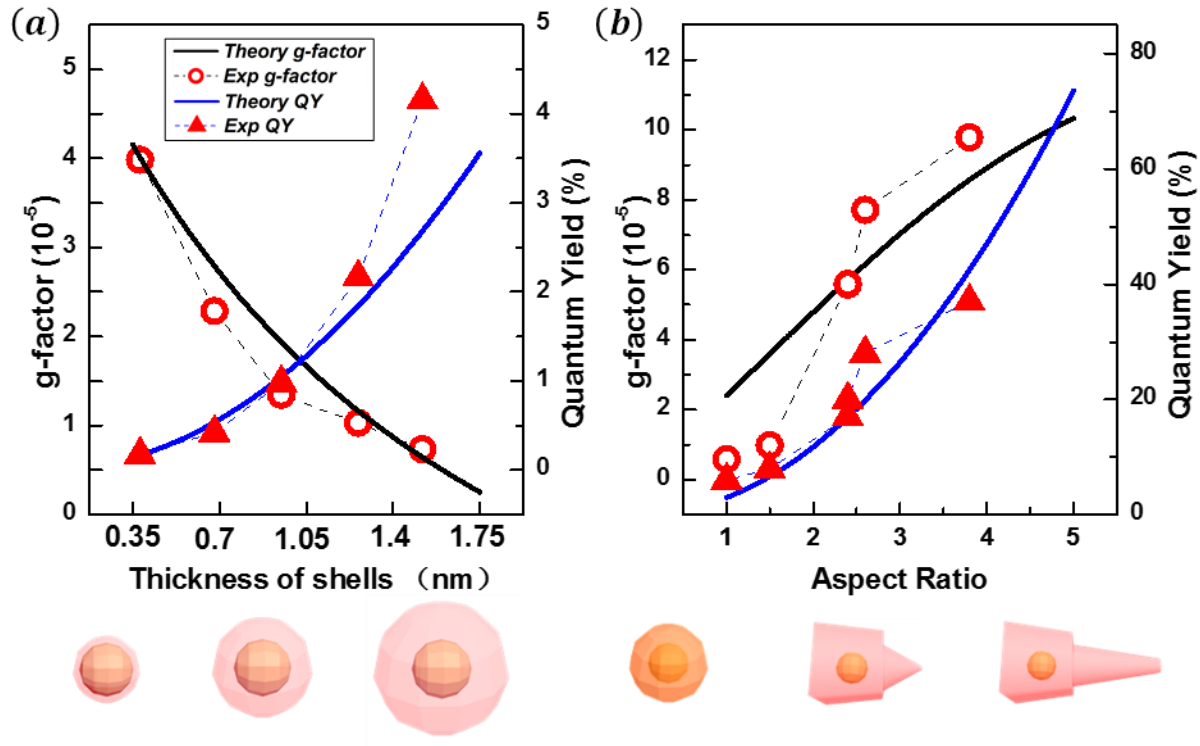

Figure 9. (a) Theoretical calculations of the spherical CdSe/CdS fitted with the experimental data. All the CdSe cores have a diameter of 2.8 nm, and we assume that one layer of CdS has a thickness of approximately 0.35 nm.[58] (b) Theoretical results fitted with the data of the tadpole morphology. The model aligns well with the experimental data, and the CD signal (*g*-factor) of tadpoles yielded a different size dependence from that of the spheres, whereas both the *g*-factor and QY have the same size dependence behavior.